The Role of Stress Distribution in Seismic Cycle Complexity of a Long Laboratory Fault

F. Paglialunga[1], F. Passelègue[1], JP. Ampuero[1], S. Latour[2], M. Violay[3]

[1]Université Côte d'Azur, CNRS, Observatoire de la Côte d'Azur, IRD, Géoazur, Sophia Antipolis, France
[2]Université de Toulouse, CNRS, Observatoire Midi-Pyrénées, IRAP, Toulouse, France
[3]École Polytechnique Fédérale de Lausanne, Switzerland.

Key Points:

- Loading conditions strongly influence stress distribution and rupture nucleation location
- Heterogeneous fault stress promotes the transition from system-size to complex seismic cycles
- Heterogeneous stress influences rupture dynamics, leading to abrupt decelerations and delayed secondary rupture

Corresponding author: F. Paglialunga, `federica.paglialunga@geoazur.unice.fr`

Abstract

A fundamental understanding of the factors controlling the complexity of seismic cycles is crucial to advance the study of earthquake hazard and predictability. Among these factors, stress distribution and fault system size play a significant role in shaping the complex patterns of seismic behavior. This study examines how heterogeneous loading conditions influence the seismic cycles of a long experimental fault. Seismic cycles are reproduced on analog material (poly methyl methacrylate) in a biaxial apparatus while continuously monitoring the strain field near the fault. By examining the effects of stress variability on fault behavior, we identify a whole spectrum of rupture outcomes, ranging from periodic, system-wide failures to complex seismic sequences comprising several partial ruptures before a complete event. Additionally, the resulting heterogeneous initial stress conditions before each event significantly influence their rupture dynamics, leading to abrupt rupture slowdown and subsequent delayed re-nucleation. The results provide a framework for understanding the evolution of stress heterogeneity along natural faults and its implications for earthquake predictability and rupture dynamics.

Plain Language Summary

Earthquakes present a serious threat to our society, causing loss of life and economic damage. Understanding what controls their occurrence (i.e., the seismic cycle) is essential for effective hazard assessment. However, natural faults are difficult to study directly, and their geometry and stress conditions are often unknown. To address this, we develop an experimental study that simulates seismic activity on a long artificial fault, simplifying the system for a better understanding. Using a high-frequency acquisition system, we were able to monitor the stress evolution along the fault and emphasize the importance of its distribution. In particular, heterogeneous stress along the fault was found (i) to cause complex seismic sequences, with multiple partial events occurring between major ruptures, and (ii) to strongly affect the dynamics of individual ruptures.

1 Introduction

Understanding the relationship between along-fault stress distribution and fault behavior is a fundamental challenge in earthquake science, with significant implications for seismic hazard assessment. Natural fault systems are controlled by many interacting factors that govern rupture nucleation, propagation, and arrest. Among these factors, initial along-fault stress distribution is a key driver of rupture dynamics, influencing seismic events' size, recurrence interval, and spatial characteristics. Das & Aki (1977) demonstrated that a stress barrier can affect the rupture dynamics and the general complexity of slip profiles. Caniven et al. (2017) showed through an analog model how spatial variations of fault normal stress *'control the ability of the fault to generate irregular or regular seismic cycles and produce clustering sequences'*. Such complex seismic cycles are also known as supercycles (Salditch et al., 2020).

Together with stress heterogeneity, another key aspect that contributes to the seismic cycle complexity is the system size. In particular, the ratio between the fault length L and the cohesive zone size L_c is pivotal. For large $\frac{L}{L_\mathrm{c}}$, Lapusta & Rice (2003) highlighted the emergence of partial ruptures between complete events that break the whole fault, sharing similar nucleation characteristics. Cattania (2019) demonstrated that a larger ratio $\frac{L}{L_\mathrm{c}}$ leads to complex earthquake sequences even along planar faults with homogeneous frictional properties when driven by the heterogeneous loading imposed by fault creep outside the seismogenic zone. The occurrence of partial events implies the arrest of a propagating rupture. This condition is favored in long fault systems (Ke et al., 2020) and is expected to be enhanced by heterogeneous stress distributions (Tinti et al., 2005; Radiguet et al., 2013, 2015; Bayart et al., 2018; S. B. Cebry et al., 2023).

However, studying the role of stress heterogeneity in seismic behavior is complexified because earthquakes typically occur at great depths. Except for rare cases (Bakun et al., 2005), instrumenting faults and gaining insights into their loading and geometrical conditions remains challenging. One promising solution is replicating earthquakes on artificial faults in controlled laboratory settings equipped with advanced acquisition systems. While simplifying natural fault systems, especially their rheology and geometry, this approach allows investigation of many key aspects of seismic activity, leading to valuable insights into earthquake physics and mechanics (Brace & Byerlee, 1966; Rosakis et al., 1999; Xia et al., 2004; Lu et al., 2007; G. C. Mclaskey & Kilgore, 2013; Svetlizky & Fineberg, 2014; Passelègue et al., 2014; Bayart et al., 2018; G. Mclaskey, 2019; Selvadurai, 2019; Rubino & Rosakis, 2020; Chen et al., 2021; Gvirtzman & Fineberg, 2021; Tal et al., 2022; Rubino et al., 2022; Mastella, 2022; S. B. Cebry et al., 2023; Corbi, 2024; Fryer et al., 2024).

Large-scale friction experiments on rocks have so far unveiled important features of laboratory earthquakes (Dieterich, 1978, 1981; Okubo & Dieterich, 1981, 1984; Yamashita et al., 2018, 2021; Ke et al., 2018, 2020). However, despite their significant size, their ratio L/L_c remains small compared to what is expected in nature. Using analog materials, which have smaller elastic moduli and critical slip distances than rocks, allows for an increase in the $\frac{L}{L_c}$ ratio by an order of magnitude compared to rock fault interfaces (Rosakis et al., 1999; Latour et al., 2013; Svetlizky & Fineberg, 2014; Svetlizky et al., 2017; Bayart et al., 2016, 2018; Guérin-Marthe et al., 2019; Gounon et al., 2022; S. B. L. Cebry et al., 2022; Rubino et al., 2022). In this study, we present new experimental results highlighting the influence of heterogeneous stress distributions on the seismic behavior of a laboratory fault with an unprecedented $\frac{L}{L_c} \sim 100$. Our results demonstrate that a heterogeneous loading can (i) affect the nucleation location of instabilities, (ii) increase the number of partial events occurring between complete ruptures, and (iii) induce complex dynamic rupture propagation processes.

2 Experimental setup and methods

A large biaxial apparatus was built in the Laboratory of Experimental Rock Mechanics at the Swiss Federal Institute of Technology of Lausanne (EPFL), allowing for a ratio of $\frac{L}{L_c}$ ~100. In a direct single-shear configuration, two samples are pressed together and successively sheared to produce frictional ruptures. This setup hosts analog material samples (2.5 x 0.5 x 0.03 m) that can slip along a 2.5 x 0.03 m artificial interface (Figure 1a, Figure S1). The samples are made of polymethylmethacrylate (PMMA), characterized by S-wave velocity $C_s = 1350$ m/s and P-wave velocity $C_d = 2700$ m/s. The normal load is applied via twenty hydraulic pistons across four distribution plates. Shear load is applied by five pistons, uniformly loading the bottom sample's lateral side at an elastic loading rate of 0.44 MPa/s (Figure 1a).

Strain evolution along the fault was monitored using strain gauges at 40 kHz recording frequency. Rosettes were placed ~3 mm from the fault at nine locations, with eight usable simultaneously (Figure 1a). Stress tensors were derived assuming plane stress conditions (see supplementary material for details). Five stopper configurations were used (Figure 1a) to modify external loading and influence stress distribution along the fault (Iwashita et al., 2023). The first used a 50 cm stopper spanning the full sample height, referred to as the "large stopper" (green). The second and third used a 20 cm stopper placed at 28 cm ("top-medium stopper", yellow) and 9 cm ("bottom-medium stopper", blue) from the fault. The fourth and fifth used an 8.5 cm stopper at 38 cm ("top-small stopper", purple) and 9 cm ("bottom-small stopper", orange) from the fault.

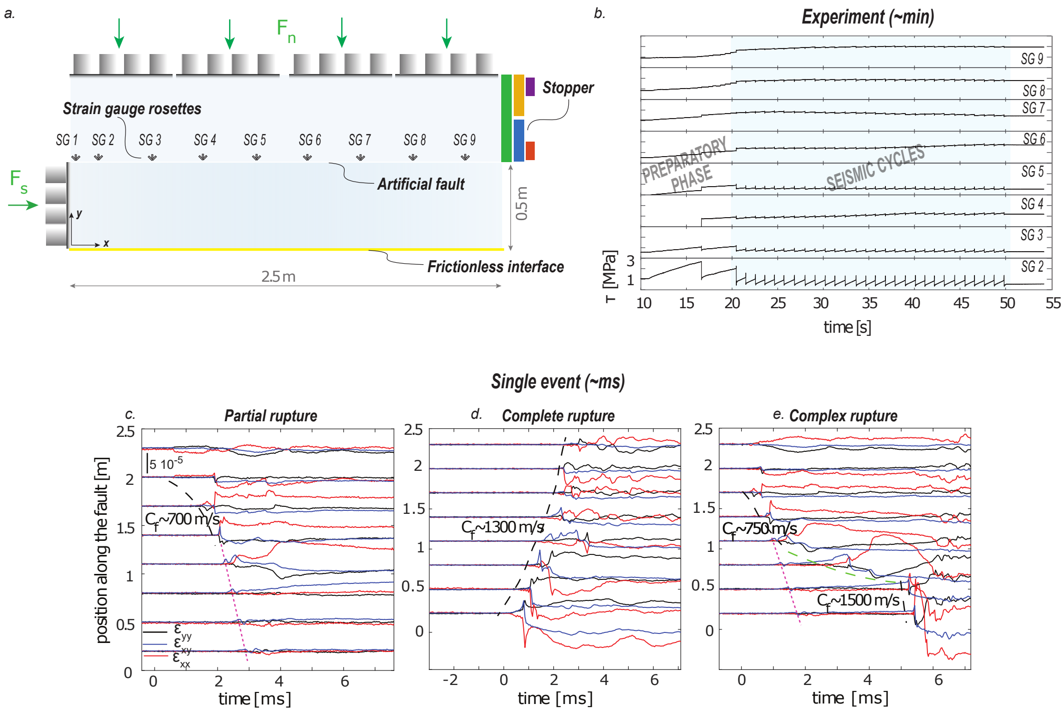

Figure 1. (a) Sketch of the large biaxial apparatus. Different stoppers are indicated by distinct colors. (b) Temporal evolution of shear stress (τ) throughout one representative experiment, at eight measuring locations (SG1-SG8). Strain measurement during (c) partial, (d) complete, and (e) complex events. Solid black, blue, and red curves indicate the vertical, shear, and horizontal strains, respectively. Black dashed lines indicate the rupture propagation front, purple dotted curves the S-wave velocity, and green dashed curves the strain transfer.

3 Results

3.1 Laboratory earthquakes

Across all experiments conducted, the fault behavior exhibited rich and yet reproducible sequences of rupture events. The fault accommodated the shear stress increase through a preparatory phase involving several partial ruptures (Rubinstein et al., 2004; Kammer et al., 2015), followed by a sequence of recurrent seismic cycles, including ruptures that propagated along the entire fault length (Figure 1b).

Three principal types of events were identified: partial (Figure 1c), complete (Figure 1d), and complex ruptures (Figure 1e). Partial ruptures predominantly nucleated on the right side of the fault (near x= 2.3 m, where x is the position along the fault relative to the left edge of the sample), accelerated into dynamic propagation (dashed black lines). They reached a speed of $\sim$ 700 m/s ($\simeq 0.52C_{\mathrm{s}}$), then decelerated and arrested before reaching the sample's edge. The arrest caused localized strain accumulation in the unruptured region (Figure 1c). Complete ruptures nucleated at the left edge of the fault (x= 0 m) and dynamically propagated across the entire fault at an average rupture velocity of $\sim$ 1250 m/s ($\sim C_{\mathrm{r}}$) (Figure 1d). However, the majority of complete ruptures exhibited complex dynamics (Figure 1e). These events generally nucleated near x= 2.3 m and promptly accelerated to a speed of $\sim$ 750 m/s. The rupture front was halted at position x=1.1 m, resulting in a slow but continuous strain accumulation over 0.5 m. It then re-nucleated and propagated through the remaining fault length at supershear velocity ($\sim$ 1500 m/s).

3.2 Influence of initial stress distribution on rupture nucleation

The nucleation location of complete ruptures was determined and analyzed for each experiment. We focused on complete ruptures, as partial ones consistently nucleated on the right side of the fault, in line with previous, extensively studied observations (Rubinstein et al., 2011; Kammer et al., 2015). The distributions of $\frac{\tau}{\sigma_{\mathrm{yy}}}$ before each rupture event, interpolated between the measurement locations, are shown by the gray solid lines in Figure 2.

Our results confirm that the external boundary conditions control the rupture nucleation locations. When the large or the top-small stopper was employed, all ruptures consistently nucleated on the right side (Figures 2a, e). Notably, with the top-small stopper, the average nucleation location shifted slightly toward the central part of the fault (Figure 2e). In contrast, other stopper configurations resulted in nucleation occurring on both the left and right sides (Figures 2b-d). For the top-medium stopper, 62% of the events nucleated on the right side, while 38% occurred on the left. The bottom-medium stopper exhibited the most balanced distribution, with nearly 50% of events nucleating on each side of the fault. Lastly, the bottom-small stopper predominantly induced nucleation on the right side, with only 22% of complete ruptures originating on the left.

A representative friction profile recorded before an event nucleating on the right (left) side is shown as solid (dashed) colored lines. At first order, the nucleation occurs where $\frac{\tau}{\sigma_{\mathrm{yy}}}$ reaches its largest value. Right-side nucleation events coincided with the highest $\frac{\tau}{\sigma_{\mathrm{yy}}}$ values, measured as 0.41, 0.44, 0.52, and 0.38 for the large stopper, top-medium stopper, bottom-medium stopper, and top-small stopper, respectively (solid colored lines, Figures 2a-d). This trend was confirmed for events nucleating on the left side in experiments where strain gauge data were available on that portion of the fault. For instance, with the top-small stopper configuration, left-side ruptures nucleated at a local $\frac{\tau}{\sigma_{\mathrm{yy}}}$ value of 0.59 (Figure 2d, dashed orange curve).

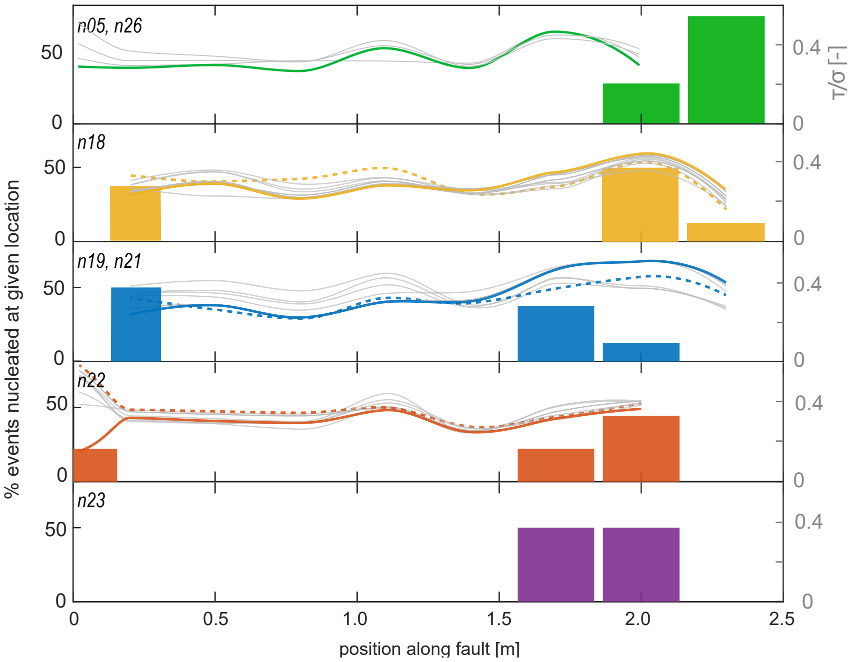

Figure 2. Distribution of event nucleation locations along the fault for different initial boundary conditions. Color legend refers to Figure 1. In gray the distribution of $\frac{\tau}{\sigma_{\mathrm{yy}}}$ before each studied. In colored solid lines and dashed line the distribution before selected ruptures nucleating on the right and left side of the fault.

3.3 From system-size events to complex seismic sequences

The observed seismic sequences exhibited a wide range of behaviors, from regular complete ruptures to complex seismicity patterns. For each event, the rupture length was determined based on the fault segment that exhibited a sudden shear stress drop, a hallmark of rupture propagation (Figure 3a). The resolution of these measurements depends on the spatial arrangement of the strain gauges along the fault.

External loading conditions exerted by the different stopper configurations controlled the complexity of the seismic sequences. Experiments with large stopper revealed the most diverse rupture size distribution, with an average of six partial ruptures occurring between two complete ruptures (Figure 3a). In contrast, experiments with top-medium stopper yielded an average of two partial ruptures between consecutive complete ruptures. Experiments conducted with bottom-medium stopper were predominantly characterized by system-size events, consisting of single complete ruptures occurring at regular intervals. Bottom-small stopper experiments exhibited a more complex distribution, with an average of four partial ruptures occurring between two complete ruptures. Finally, experiments involving top-small stopper were dominated by periodic complete ruptures.

The patterns of inter-event times provide further insight into how the stress distribution influences the complexity of the seismic cycle. We define two distinct time intervals (Gualandi et al., 2023): $T_{\mathbf{pre}}$ is the time elapsed between a given event and the one preceding it, and $T_{\mathbf{next}}$ is the time between an event and the subsequent one. For events occurring periodically $T_{\mathbf{pre}} = T_{\mathbf{next}}$, while for events not occurring periodically $T_{\mathbf{pre}} \neq T_{\mathbf{next}}$. This analysis was performed for each external loading condition by considering (i) complete events only (Figure 3c) and (ii) all events, including both partial and complete ruptures (Figure 3c). The inter-event times between complete events show almost periodic behavior (with values ranging between 2 and 6 seconds, Figure 3d). The only exception is an example of cycle skipping in experiment n19 (in blue in Figure 3), where the second expected complete rupture was instead a slow slip event, without the sharp and pronounced stress drop observed in fast rupture events (Figure S2). When considering the totality of events (Figure 3b), the inter-event times ranged between 0.1 and 1.5 s for the complex sequences (n26, n18, and n22) and between 2.1 and 3.5 s for the system-size sequences (n19, n23). Many of them, mostly partial ruptures, occurred periodically (Figure 3d). This happened for 70%, 21%, 50%, 42%, and 100% of the total number of events respectively for n26, n18, n19, n22, n23).

Interestingly, the inter-event times of the events that deviate from periodicity, tend to cluster along different slopes, suggesting that the fault behavior tends towards a periodic pattern. This is evident for experiment n18, where the second, third, and fourth sequences follow a similar pattern: a longer interval after a complete rupture, followed by two shorter intervals after partial ruptures. A similar trend is observed in experiment n22. In these events, the inter-event time seems governed by the static friction drop experienced by the preceding rupture at the nucleation site. Larger friction drops lead to longer inter-event times (Figure S3). Notably, the large static friction drops associated with complete ruptures are influenced by post-seismic activity, such as secondary ruptures and wave reflections, which is absent or minimal in the case of partial ruptures. These processes further weaken the fault, resulting in a larger static stress drop. At the same time, such post-seismic activity delays the fault's re-locking and subsequent re-loading. The magnitude of this effect depends on the stress distribution, leading to a range of $\frac{T_{\mathbf{next}}}{T_{\mathbf{pre}}}$ values between 1 and 4.

4 Discussion

4.1 On the emergence of complex seismic cycles

The initial stress distribution controlled the nucleation location of the rupture events, which occurred at different positions along the fault. In particular, the nucleation locations were correlated with the local stress ratio $\frac{\tau}{\sigma_{\mathrm{yy}}}$, and occurred consistently at the places where it was maximal. This observation is consistent with previous studies that highlight that rupture nucleation tends to occur where $\frac{\tau}{\sigma_{\mathrm{yy}}}$ is maximal (Ben-David & Fineberg, 2011). However, we also observed that the values of $\frac{\tau}{\sigma_{\mathrm{yy}}}$ at nucleation were not fixed but ranged between 0.35 and 0.6 (values sensitive to the spatial resolution of our measurements). So, while $\frac{\tau}{\sigma_{\mathrm{yy}}}$ plays a key role in controlling the onset of rupture, it is not a sufficient nucleation criterion. In fact, nucleation models show that other quantities can contribute significantly; for example, potential and fracture energies control nucleation through quasi-static crack growth in the large-scale yield regime (e.g. Rubin & Ampuero, 2005).

The heterogeneous stress distribution not only influenced rupture nucleation but also shaped the overall seismic cycle, leading to the emergence of finite rupture events between complete ruptures. The seismicity statistics surrounding a major event are generally explained by the frictional properties of faults (Kaneko et al., 2010; Dublanchet et al., 2013; Wang et al., 2024) or geometrical characteristics (Dal Zilio et al., 2019), but even a single homogeneous fault can exhibit complex behavior if sufficiently long (Cattania, 2019). Our experiments integrate these conditions. The seismic cycles occurred on a single fault (L=2.5 m) approximately 100 times larger than the expected nucleation length (L_{c}=2.5 cm (Latour et al., 2013; Paglialunga et al., 2023)). According to Cattania (2019), such a high $\frac{L}{L_{\mathrm{c}}}$ ratio is sufficient to induce the occurrence of sub-system-size events in the presence of a heterogeneous loading.

More precisely, the emergence of partial ruptures can be explained through an energetic perspective. In Linear Elastic Fracture Mechanics, rupture propagation occurs

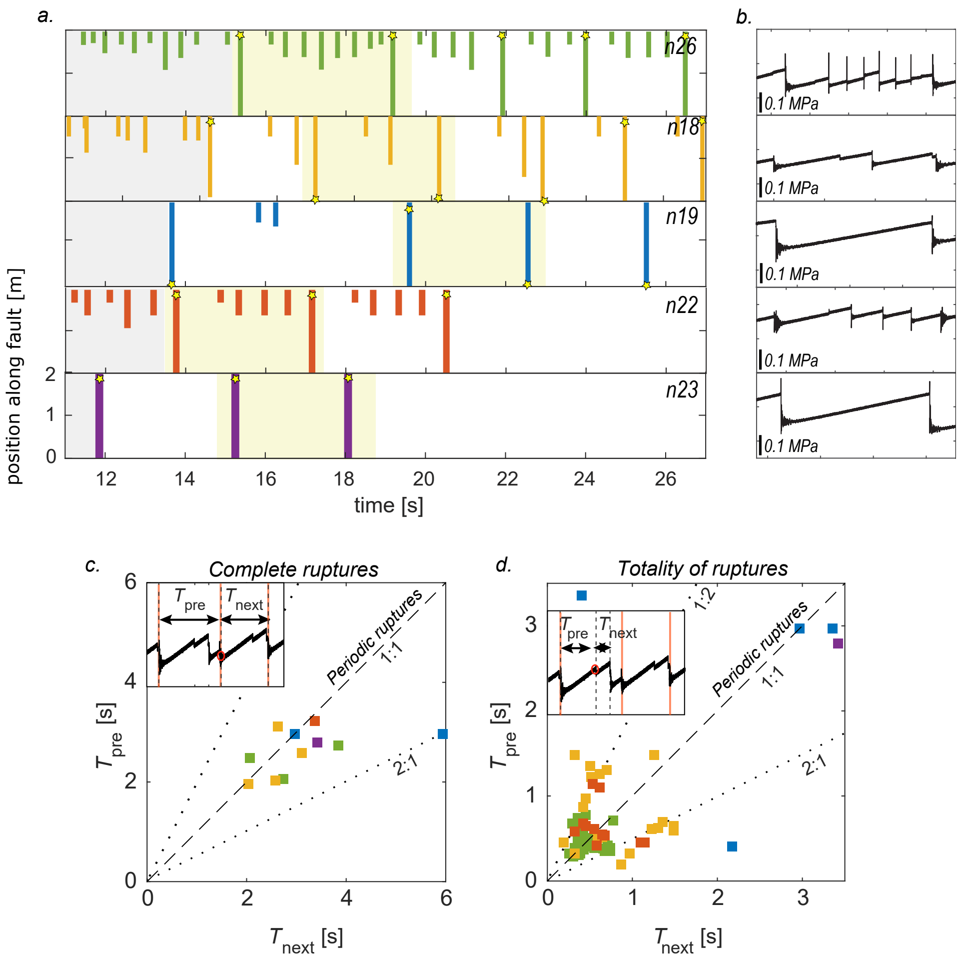

Figure 3. (a) Occurrence time and rupture length for all the events in selected experiments (from top to bottom: n26, n18, n19, n22, n23). Due to sensor placement, complete ruptures spanning the full 2.5 m fault appear as 2 m long. Stars indicate the nucleation location of complete ruptures. The gray area indicates the preparatory phase before first complete event. The yellow area indicates the selected sequences shown in (b). (b) Shear stress evolution for a representative seismic sequence, measured by strain gauge SG7 (x=1.7 m). Inter-event times are computed (c) for complete ruptures only and (d) for all events, partial and complete. Color legend follows the one indicated in Figure 1.

when the energy release rate (G) at the rupture tip exceeds the fracture energy (G_c), which resists rupture propagation (Freund, 1979). If the available energy is insufficient, the rupture will arrest. This can occur due to either a reduction in G or an increase in G_c. In our experimental seismic sequences, multiple ruptures sequentially arrested when the energy release rate fell below the fracture energy ($G < G_c$) (Figure S5). This arrest increased shear stress in the unruptured section of the fault, raising the energy available for subsequent ruptures (Figures S5d-e). Eventually, this process led to full rupture propagation once G exceeded G_c along the entire fault. This analysis aligns with previous rupture length predictions (Kammer et al., 2015; Bayart et al., 2016; Ke et al., 2018) (see supplementary material).

The temporal evolution of stress during the sequence shows that, as the shear stress approaches its critical distribution (represented by the bright green curve in Figure S5c), the local stress increase generated by the arrest of the previous partial rupture becomes progressively smaller. This process culminates in an almost imperceptible rise, ultimately leading to a complete rupture. This phenomenon is illustrated by the near overlap of stress distributions immediately before the complete and preceding partial ruptures (Figure S4). Additionally, the stress distribution converges toward the critical state, and the partial events preceding a complete rupture exhibit similar propagation phases (Figure S4), as previously observed in numerical studies (Lapusta & Rice, 2003). This behavior aligns with natural observations of similar initiation of small and large earthquakes (Bouchon et al., 2011; Meier et al., 2017). As the fault state approaches its critical conditions, predicting the timing of the main event becomes increasingly challenging.

Our experiments also provide valuable insight into interevent times. For complex sequences, when considering all events, their occurrence seems aperiodic, with inter-event times ranging from 0.1 to 3.3 seconds (Figure 3d). However, a closer examination reveals a tendency of the fault toward periodic patterns. In particular, most partial ruptures occurred periodically, whereas complete ruptures often resulted in longer interevent times. This behavior is governed by the heterogeneous stress distribution along the fault, as previously observed in experimental fault systems (Caniven et al., 2017). This phenomenon has also been employed as an indirect method for mapping seismic asperities in space (Wyss et al., 2000). In contrast, complete ruptures exhibit overall periodic recurrence, with inter-event times of 2 to 6 seconds (Figure 3c). Their coefficient of variation, defined as $\mathrm{CV}(\%) = \left(\frac{\mathrm{SD}}{\bar{x}}\right)\times 100$, where SD is the standard deviation and $\bar{x}$ the mean value, was calculated. The resulting CV were 23%, 18.6%, 39.9%, 6%, and 23.5% respectively for experiments n26, n18, n19, n22, n23. The cycles involving only system-size events (associated with lower stress heterogeneity) tend to have slightly longer average recurrence times compared to cycles with multiple ruptures (associated with higher stress heterogeneity). This finding is consistent with the simulations of Cattania & Segall (2021), which show that rough faults exhibit longer recurrence times than smooth ones, suggesting that fault properties and stress heterogeneity may exert similar effects on periodicity. Our observation highlights that the on-fault stress distribution dictates a first-order recurrence time (Figure 3c). The latter can, however, be modulated (lengthened or shortened) by the emergence of partial ruptures or slow slip events controlled by local stress heterogeneities.

4.2 Influence of stress heterogeneity on rupture dynamics

Most complete ruptures observed in these experiments exhibit *complex* rupture processes (Figure 1e). They generally nucleated near the leading edge and accelerated to a rupture speed of approximately 0.5 C_s. After propagating over 50 cm, they decelerated to transient velocities ranging from 650 m/s to 56 m/s, depending on the event, over 0.9 m. This slowdown occurred in a stress barrier region where the available energy was lower (Figure S5d). The transient propagation of the rupture within this low-stressed region was accompanied by a stress build-up over a period defined as t_{delay} (Figure 4).

Following this delay, a new rupture was dynamically triggered, propagating at supershear velocities.

The measured rupture delay time t_{delay} (calculated as the time interval between two distinct and sudden stress drops), varied significantly across the different complex ruptures observed, spanning more than an order of magnitude, from 1.4 to 18 ms (Figure 4). The duration t_{delay} appears to be controlled by the initial level of stress along the barrier, before the transient rupture propagation. Effectively, for each loading condition, t_{delay} decreases linearly with $\Delta\tau_{\text{delay}}$, defined as $\tau_{\text{arrest}}-\tau_{\text{res}}$, with τ_{arrest} the shear stress at the arrest location before the stress build-up caused by the transient rupture propagation, and τ_{res} the residual stress level achieved along the fault after the transient rupture propagation. Large values of $\Delta\tau_{\text{delay}}$ induce faster transient rupture velocities within the stress barrier, resulting in shorter t_{delay}. Note that $\Delta\tau_{\text{delay}}$ serves as a direct proxy for the efficiency of the barrier: a large (small) $\Delta\tau_{\text{delay}}$ indicates an initial stress state close to (far from) the fault frictional strength.

To investigate further, numerical simulations were performed using the spectral element software SEM2DPACK (Ampuero, 2012; Ampuero et al., 2024). An exponential slip-weakening friction law was used and justified by previous experimental observations highlighting a continued shear stress weakening with slip (Paglialunga et al., 2024). The critical slip distance, the static and residual friction, as well as the initial stress distribution were extrapolated from experimental observations (i.e., heterogeneous distribution, Figure S9). A low shear stress zone was imposed to reflect the observed stress drop barrier (Figure S8). This locally generated friction value lower than the residual strength, causing the rupture to slow down or arrest. The nucleation was forced through a region of overstress imposed at x=1.76 m, as in the experimental event. The numerical simulation qualitatively reproduced the experimental observations, capturing a similar complex rupture propagation process (Figure 4). Upon nucleation, the rupture propagated bilaterally. The rightward-propagating front exhibited a variable subshear velocity until it reached the fault edge. The leftward-propagating front initially traveled at a subshear velocity but briefly transitioned to supershear before encountering the stress drop barrier. At this point, the rupture decelerated abruptly, radiating stopping waves (Figure 4e) that reduced slip velocity in the wake of the rupture tip. Additionally, S-waves were radiated ahead of the rupture front (Figure 4f). Within the stress drop barrier, the rupture did not fully arrest, instead, it propagated at a significantly reduced velocity. This creeping front was governed by continued weakening under the exponential slip-weakening law and was accompanied by a shear stress increase ahead of the rupture tip (Figure 4f, where the light blue area contrasts with the initial dark blue area indicating the barrier). Moreover, S-waves previously radiated by the rupture were reflected at the fault edges. Upon re-entering the barrier, these reflected waves locally enhanced slip through a step-like increase. This gradual yet persistent rise in stress enabled the rupture to overcome the stress drop barrier, eventually reaching a shear stress level sufficient to resume dynamic propagation (Figure S10).

This numerical simulation qualitatively replicates the experimental conditions, providing valuable insights into the interpretation of our observations. It underscores the significant influence of a stress barrier on rupture dynamics, which can markedly alter the propagation behavior without necessarily stopping the rupture. This behavior arises when the governing friction law incorporates continued weakening, as demonstrated by the exponential slip-weakening law used in this study. Continued slip-weakening has already proven to be a highly effective mechanism for rupture propagation across stress barrier (Paglialunga et al., 2022). This process bears similarities to the observed creep fronts in laboratory experiments on analog materials containing quartz gouge faults (S. B. L. Cebry et al., 2022). However, in those experiments, delayed triggering was attributed to a combination of initial overstress and the frictional properties of the gouge. These observations collectively highlight how the transition from partial to complex events can

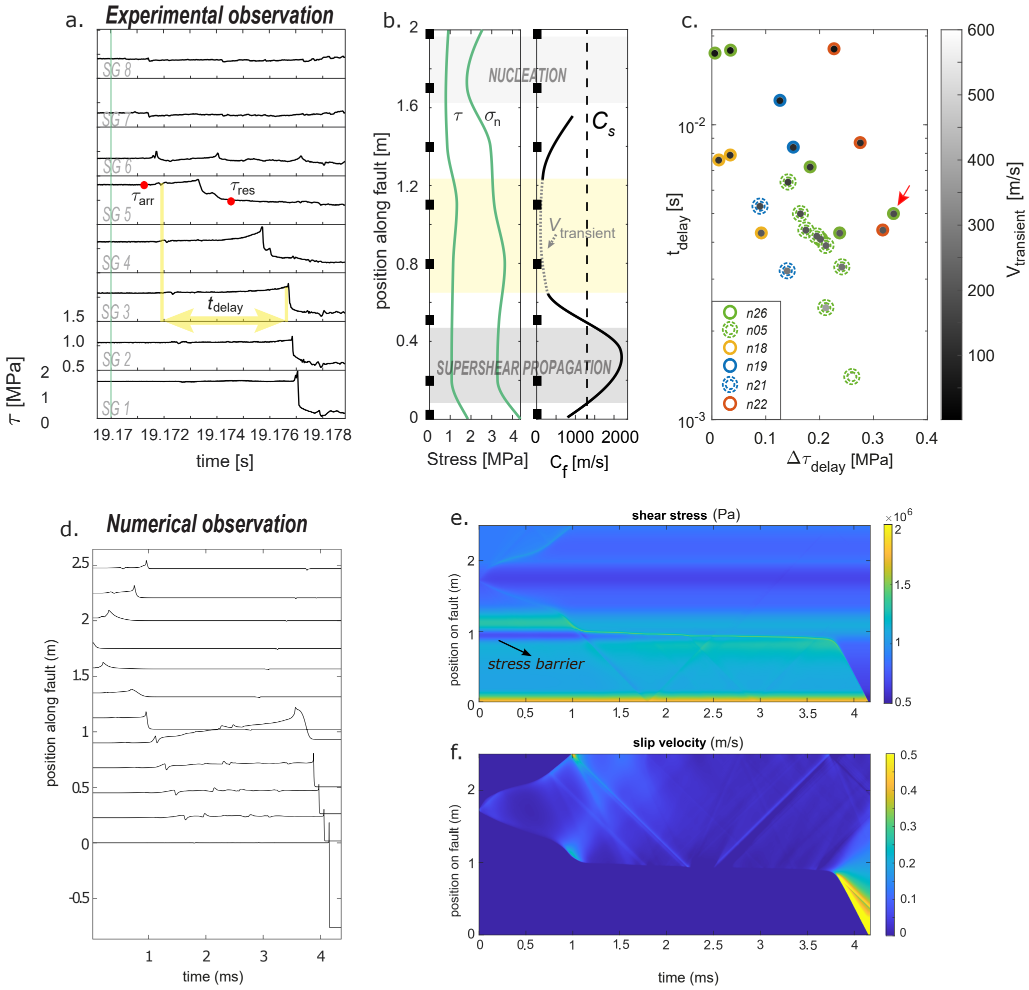

Figure 4. (a) Temporal shear stress evolution at all gauges, with time delays highlighted in yellow and red markers for τ_{arr} and τ_{res}.(b) Stress distribution before the event (green line) and rupture speed. (c) t_{delay} and $\Delta\tau_{\mathrm{delay}}$ for all ruptures, showing a linear trend within experiments, indicating stress controls delay and velocity. The red arrow points to the event in (a). (d) Numerical simulation of complex rupture. Temporal evolution of shear stress at equidistant fault locations. (e, f) Spatiotemporal evolution of slip velocity and shear stress.

be very abrupt. One could argue that these complex ruptures correspond to two distinct seismic events. The time delay between the two propagation phases is one to two orders of magnitude larger than the early dynamic propagation phase. This result questions the definition of the rupture event itself, where the second propagation phase could be interpreted as an early aftershock or, if of comparable size, as a doublet earthquake (Sladen et al., 2010). In our simulation, the critical slip distance is much smaller than what expected for natural earthquakes. Increasing the fault size and D_c would enhance both the propagation time and time delay between subsequent rupture phases. Although the first is expected to increase linearly with rupture length, assuming a given rupture velocity, the second would be mainly controlled by the severity of the barrier. A deeper investigation of the relation between time delay and barrier efficiency will be subject of future work.

5 Conclusions

Our results demonstrate that heterogeneous initial stress conditions along an extended experimental fault can shift seismic cycle behavior from system-size, periodic ruptures to cycles exhibiting greater complexity. Such complexity is evident in the occurrence time of ruptures, their nucleation location, size, and inter-event time. These findings support the idea that a detailed investigation of the seismicity spatial and temporal evolution along natural fault systems could help elucidate the evolution of stress distribution. Furthermore, we highlight the pivotal role of stress heterogeneity in controlling the rupture dynamics of single events. We observed a 'complex rupture' phenomenon, marked by strong deceleration caused by stress heterogeneity, followed by re-nucleation. This behavior sheds light on the variability of seismic events, suggesting that, depending on heterogeneity strength, a rupture may either remain confined to a smaller scale or escalate into a larger event.

Open Research Section

The data used in this study will be publicly available at 10.5281/zenodo.15167862 Temporal access is granted for the review time (see link in data file).

The numerical code used to simulate dynamic rupture propagation is SEM2DPACK (Ampuero, 2012), an open-source research code available at https://github.com/jpampuero/sem2dpack.

Acknowledgments
F.P. and M.V. acknowledge support from the European Research Council Starting Grant project 757290-BEFINE. F.P. and F.P. acknowledge support from the European Research Council Starting Grant project HOPE 101041966. J.P.A. is supported by the French government, through the UCAJEDI Investments in the Future project (ANR-15-IDEX-01) managed by the National Research Agency (ANR).

References

Ampuero, J. P. (2012). Sem2dpack, a spectral element software for 2d seismic wave propagation and earthquake source dynamics, v2.3.8. *Zenodo*. doi: 10.5281/zenodo.230363

Ampuero, J. P., Currie, T. W., Herrera, M. T., Huang, Y., Lestrelin, H., Liang, C., ... Weng, H. (2024). jpampuero/sem2dpack: Sem2dpack v2.3.9 (sem2dpack_2.3.9). *Zenodo, [software]*. doi: 10.5281/zenodo.13821494

Bakun, W., Aagaard, B., Dost, B., Ellsworth, W. L., Hardebeck, J. L., Harris, R. A., ... others (2005). Implications for prediction and hazard assessment from the 2004 parkfield earthquake. *Nature*, *437*(7061), 969–974.

Bayart, E., Svetlizky, I., & Fineberg, J. (2016). Fracture mechanics determine the lengths of interface ruptures that mediate frictional motion. *Nature Physics*, *12*(2), 166–170. doi: 10.1038/nphys3539

Bayart, E., Svetlizky, I., & Fineberg, J. (2018). Rupture Dynamics of Heterogeneous Frictional Interfaces. *Journal of Geophysical Research: Solid Earth*, *123*(5), 3828–3848. doi: 10.1002/2018JB015509

Ben-David, O., & Fineberg, J. (2011). Static friction coefficient is not a material constant. *Physical Review Letters*, *106*(25), 1–4. doi: 10.1103/PhysRevLett.106.254301

Bouchon, M., Karabulut, H., Aktar, M., Özalaybey, S., Schmittbuhl, J., & Bouin, M.-P. (2011). Extended nucleation of the 1999 m w 7.6 izmit earthquake. *science*, *331*(6019), 877–880.

Brace, W. F., & Byerlee, J. D. (1966). Stick-Slip as a Mechanism for Earthquakes. *Science*, *153*(3739), 990–992. Retrieved from `https://science.sciencemag.org/content/153/3739/990` doi: 10.1126/science.153.3739.990

Caniven, Y., Dominguez, S., Soliva, R., Peyret, M., Cattin, R., & Maerten, F. (2017). Relationships between along-fault heterogeneous normal stress and fault slip patterns during the seismic cycle: Insights from a strike-slip fault laboratory model. *Earth and Planetary Science Letters*, *480*, 147–157.

Cattania, C. (2019). Complex Earthquake Sequences On Simple Faults. *Geophysical Research Letters*, *46*(17-18), 10384–10393. doi: 10.1029/2019GL083628

Cattania, C., & Segall, P. (2021, 4). Precursory slow slip and foreshocks on rough faults. *Journal of Geophysical Research: Solid Earth*, *126*. doi: 10.1029/2020JB020430

Cebry, S. B., Sorhaindo, K., & McLaskey, G. C. (2023). Laboratory earthquake rupture interactions with a high normal stress bump. *Journal of Geophysical Research: Solid Earth*, *128*(11), e2023JB027297.

Cebry, S. B. L., Ke, C.-y., Shreedharan, S., Marone, C., Kammer, D. S., & Mclaskey,

G. C. (2022). Creep fronts and complexity in laboratory earthquake sequences illuminate delayed earthquake triggering. *Nature Communications*, 1–9. doi: 10.1038/s41467-022-34397-0

Chen, X., Chitta, S. S., Zu, X., & Reches, Z. (2021). Dynamic fault weakening during earthquakes: Rupture or friction? *Earth and Planetary Science Letters*, *575*, 117165. Retrieved from `https://doi.org/10.1016/j.epsl.2021.117165` doi: 10.1016/j.epsl.2021.117165

Corbi. (2024). Asperity size and neighboring segments can change the frictional response and fault slip behavior: Insights from laboratory experiments and numerical simulations. *Journal of Geophysical Research: Solid Earth*, *129*(1), e2023JB026594.

Dal Zilio, L., van Dinther, Y., Gerya, T., & Avouac, J. P. (2019). Bimodal seismicity in the Himalaya controlled by fault friction and geometry. *Nature Communications*, *10*, 1–11. Retrieved from `http://dx.doi.org/10.1038/s41467-018-07874-8` doi: 10.1038/s41467-018-07874-8

Das, S., & Aki, K. (1977). Fault plane with barriers: A versatile earthquake model. *Journal of Geophysical Research*, *82*(36), 5658–5670. doi: 10.1029/jb082i036p05658

Dieterich, J. H. (1978). Preseismic Fault Slip and Earthquake Prediction. *Journal of Geophysical Research*, *83*(8), 3940–3948. doi: 10.1029/JB083iB08p03940

Dieterich, J. H. (1981). Potential for Geophysical Experiments in Large Scale Tests. *Geophysical Research Letters*, *8*(7), 653–656. doi: 10.1029/GL008i007p00653

Dublanchet, P., Bernard, P., & Favreau, P. (2013). Interactions and triggering in a 3-D rate-and-state asperity model. *Journal of Geophysical Research : Solid Earth*, *118*(April), 2225–2245. doi: 10.1002/jgrb.50187

Freund, L. B. (1979). The mechanics of dynamic shear crack propagation. *Journal of Geophysical Research: Solid Earth*, *84*(B5), 2199–2209. doi: 10.1029/JB084iB05p02199

Fryer, B., Lebihain, M., Noël, C., Paglialunga, F., & Passelègue, F. (2024). The effect of stress barriers on unconventional-singularity-driven frictional rupture. *Journal of the Mechanics and Physics of Solids*, *193*, 105876. Retrieved from `https://www.sciencedirect.com/science/article/pii/S0022509624003429` doi: https://doi.org/10.1016/j.jmps.2024.105876

Gounon, A., Latour, S., Letort, J., & El Arem, S. (2022). Rupture Nucleation on a Periodically Heterogeneous Interface. *Geophysical Research Letters*, *49*(20). doi: 10.1029/2021gl096816

Gualandi, A., Faranda, D., Marone, C., Cocco, M., & Mengaldo, G. (2023, 2). Deterministic and stochastic chaos characterize laboratory earthquakes. *Earth and Planetary Science Letters*, *604*. doi: 10.1016/j.epsl.2023.117995

Guérin-Marthe, S., Nielsen, S., Bird, R., Giani, S., & Di Toro, G. (2019). Earthquake Nucleation Size: Evidence of Loading Rate Dependence in Laboratory Faults. *Journal of Geophysical Research: Solid Earth*, *124*(1), 689–708. doi: 10.1029/2018JB016803

Gvirtzman, S., & Fineberg, J. (2021). Nucleation fronts ignite the interface rupture that initiates frictional motion. *Nature Physics*, *17*(9), 1037–1042.

Iwashita, W., Matsukawa, H., & Otsuki, M. (2023). Static friction coefficient depends on the external pressure and block shape due to precursor slip. *Scientific Reports*, *13*(1), 2511.

Kammer, D. S., Radiguet, M., Ampuero, J. P., & Molinari, J. F. (2015). Linear elastic fracture mechanics predicts the propagation distance of frictional slip. *Tribology Letters*, *57*(3). doi: 10.1007/s11249-014-0451-8

Kaneko, Y., Avouac, J. P., & Lapusta, N. (2010). Towards inferring earthquake patterns from geodetic observations of interseismic coupling. *Nature Geoscience*, *3*(5), 363–369. doi: 10.1038/ngeo843

Ke, C. Y., McLaskey, G. C., & Kammer, D. S. (2018). Rupture Termination in Laboratory-Generated Earthquakes. *Geophysical Research Letters*, *45*(23), 12,784–12,792. doi: 10.1029/2018GL080492

Ke, C.-Y., McLaskey, G. C., & Kammer, D. S. (2020). The earthquake arrest zone. *Geophysical Journal International*, *224*(1), 581–589. doi: 10.1093/gji/ggaa386

Lapusta, N., & Rice, J. R. (2003). Nucleation and early seismic propagation of small and large events in a crustal earthquake model. *Journal of Geophysical Research*, *108*, 1–18. doi: 10.1029/2001JB000793

Latour, S., Schubnel, A., Nielsen, S., Madariaga, R., & Vinciguerra, S. (2013). Characterization of nucleation during laboratory earthquakes. *Geophysical Research Letters*, *40*(19), 5064–5069. doi: 10.1002/grl.50974

Lu, X., Lapusta, N., & Rosakis, A. J. (2007). Pulse-like and crack-like ruptures in experiments mimicking crustal earthquakes. *Proceedings of the National Academy of Sciences*, *104*(48), 18931–18936.

Mastella. (2022). Foamquake: A novel analog model mimicking megathrust seismic cycles. *Journal of Geophysical Research: Solid Earth*, *127*(3), e2021JB022789.

Mclaskey, G. (2019). Earthquake Initiation From Laboratory Observations and Implications for Foreshocks. *Journal of Geophysical Research : Solid Earth*, *124*(12), 882–904. doi: 10.1029/2019JB018363

Mclaskey, G. C., & Kilgore, B. D. (2013). Foreshocks during the nucleation of stick-slip instability. *Journal of Geophysical Research: Solid Earth*, *118*(May), 2982–2997. doi: 10.1002/jgrb.50232

Meier, M.-A., Ampuero, J., & Heaton, T. H. (2017). The hidden simplicity of subduction megathrust earthquakes. *Science*, *357*(6357), 1277–1281.

Okubo, P., & Dieterich, J. (1981). Fracture energy of stick-slip events in a large scale biaxial experiment. *Geophysical Research Letters*, *8*(8), 887–890.

Okubo, P., & Dieterich, J. (1984). Effects of physical fault properties on frictional instabilities produced on simulated faults. *Journal of Geophysical Research: Solid Earth*, *89*(B7), 5817–5827. doi: 10.1029/JB089iB07p05817

Paglialunga, F., Passelègue, F., Brantut, N., Barras, F., Lebihain, M., & Violay, M. (2022). On the scale dependence in the dynamics of frictional rupture : Constant fracture energy versus size-dependent breakdown work. *Earth and Planetary Science Letters*, *584*. doi: 10.1016/j.epsl.2022.117442

Paglialunga, F., Passelegue, F., Latour, S., Gounon, A., & Violay, M. (2023). Influence of viscous lubricant on nucleation and propagation of frictional ruptures. *Journal Of Geophysical Research-Solid Earth*, *128*(4), e2022JB026090.

Paglialunga, F., Passelègue, F., Lebihain, M., & Violay, M. (2024). Frictional weakening leads to unconventional singularities during dynamic rupture propagation. *Earth and Planetary Science Letters*, *626*, 118550.

Passelègue, F. X., Goldsby, D. L., & Fabbri, O. (2014). Geophysical Research Letters. *Geophysical Research Letters*, *41*(3), 828–835. doi: 10.1002/2013GL058374 .Received

Radiguet, M., Kammer, D. S., Gillet, P., & Molinari, J. F. (2013). Survival of heterogeneous stress distributions created by precursory slip at frictional interfaces. *Physical Review Letters*, *111*(16), 1–5. doi: 10.1103/PhysRevLett.111.164302

Radiguet, M., Kammer, D. S., & Molinari, J. F. (2015). The role of viscoelasticity on heterogeneous stress fields at frictional interfaces. *Mechanics of Materials*, *80*(PB), 276–287. Retrieved from `http://dx.doi.org/10.1016/j.mechmat.2014.03.009` doi: 10.1016/j.mechmat.2014.03.009

Rosakis, A. J., Samudrala, O., & Coker, D. (1999). Cracks faster than the shear wave speed. *Science*, *284*(5418), 1337–1340. doi: 10.1126/science.284.5418.1337

Rubin, A. M., & Ampuero, J. P. (2005). Earthquake nucleation on (aging) rate and state faults. *Journal of Geophysical Research*, *110*(2), 1–24. doi: 10.1029/2005JB003686

Rubino, V., Lapusta, N., & Rosakis, A. (2022). Intermittent lab earthquakes in dynamically weakening fault gouge. *Nature*, *606*(7916), 922–929.

Rubino, V., & Rosakis, A. (2020). Spatiotemporal properties of sub-rayleigh and supershear ruptures inferred from full-field dynamic imaging of laboratory experiments. *Journal of Geophysical Research: Solid Earth*, *125*(2), e2019JB018922.

Rubinstein, S. M., Barel, I., Reches, Z., Braun, O. M., Urbakh, M., & Fineberg, J. (2011). Slip sequences in laboratory experiments resulting from inhomogeneous shear as analogs of earthquakes associated with a fault edge. *Pure and Applied Geophysics*, *168*, 2151–2166.

Rubinstein, S. M., Cohen, G., & Fineberg, J. (2004). Detachment fronts and the onset of dynamic friction. *Nature*, *430*(August), 1005–1009. doi: 10.1038/nature02861.1.

Salditch, L., Stein, S., Neely, J., Spencer, B. D., Brooks, E. M., Agnon, A., & Liu, M. (2020). Earthquake supercycles and long-term fault memory. *Tectonophysics*, *774*, 228289.

Selvadurai, P. A. (2019). Laboratory insight into seismic estimates of energy partitioning during dynamic rupture: An observable scaling breakdown. *Journal of Geophysical Research: Solid Earth*, *124*(11), 11350–11379. doi: 10.1029/2018JB017194

Sladen, A. a., Tavera, H., Simons, M., Avouac, J.-P., Konca, A., Perfettini, H., ... Cavagnoud, R. (2010). Source model of the 2007 mw 8.0 pisco, peru earthquake: Implications for seismogenic behavior of subduction megathrusts. *Journal of Geophysical Research: Solid Earth*, *115*(B2).

Svetlizky, I., & Fineberg, J. (2014). Classical shear cracks drive the onset of dry frictional motion. *Nature*, *509*(7499), 205–208. doi: 10.1038/nature13202

Svetlizky, I., Kammer, D., Bayart, E., Cohen, G., & Fineberg, J. (2017, mar). Brittle Fracture Theory Predicts the Equation of Motion of Frictional Rupture Fronts. *Physical Review Letters*, *118*(12), 125501. Retrieved from `https://link.aps.org/doi/10.1103/PhysRevLett.118.125501` doi: 10.1103/PhysRevLett.118.125501

Tal, Y., Rubino, V., Rosakis, A. J., & Lapusta, N. (2022). Dynamics and near-field surface motions of transitioned supershear laboratory earthquakes in thrust faults. *Journal of Geophysical Research: Solid Earth*, *127*(3), e2021JB023733.

Tinti, E., Spudich, P., & Cocco, M. (2005). Earthquake fracture energy inferred from kinematic rupture models on extended faults. *Journal of Geophysical Research: Solid Earth*, *110*(12), 1–25. doi: 10.1029/2005JB003644

Wang, L., Xu, S., Zhuo, Y., Liu, P., & Ma, S. (2024, 6). Unraveling the roles of fault asperities over earthquake cycles. *Earth and Planetary Science Letters*, *636*. doi: 10.1016/j.epsl.2024.118711

Wyss, M., Schorlemmer, D., & Wiemer, S. (2000, 4). Mapping asperities by minima of local recurrence time: San jacinto-elsinore fault zones. *Journal of Geophysical Research: Solid Earth*, *105*, 7829-7844. doi: 10.1029/1999jb900347

Xia, K., Rosakis, A. J., & Kanamori, H. (2004). Laboratory earthquakes: The sub-rayleigh-to-supershear rupture transition. *Science*, *303*(5665), 1859–1861.

Yamashita, F., Fukuyama, E., Xu, S., Kawakata, H., Mizoguchi, K., & Takizawa, S. (2021). Two end-member earthquake preparations illuminated by foreshock activity on a meter-scale laboratory fault. *Nature Communications*, *12*(1), 1–11. Retrieved from `http://dx.doi.org/10.1038/s41467-021-24625-4` doi: 10.1038/s41467-021-24625-4

Yamashita, F., Fukuyama, E., Xu, S., Mizoguchi, K., Kawakata, H., & Takizawa, S. (2018). Rupture preparation process controlled by surface roughness on meter-scale laboratory fault. *Tectonophysics*, *733*(September 2017), 193–208. Retrieved from `https://doi.org/10.1016/j.tecto.2018.01.034` doi: 10.1016/j.tecto.2018.01.034